Modelling of a Variable Length Gas Cell Target for Laser Wakefield Acceleration

R. Luo¹, * G. R. Christian¹, M. P. Backhouse¹, N. C. Lopes²,
S. S. Alatabi¹, M. S. Bloom¹, M. Maier³, and Z. Najmudin¹

¹ The John Adams Institute, Imperial College London, SW7 2BZ, United Kingdom

² GoLP/Instituto de Plasmas e Fusão Nuclear, Instituto Superior Técnico, 1049-001 Lisboa, Portugal and

³ Department of Mathematics, Texas A&M University, TX77843, United States of America

(Dated: September 4, 2025)

We present time-dependent 2D and 3D fluid simulations of a gas cell with a variable length of 0 to 5 cm, designed for laser wakefield acceleration. The cell employs an output nozzle producing extended density ramps, which can facilitate the production of high-quality electron beams. In both geometries, the simulations demonstrate uniform density inside the cell. In 3D, the mean density inside the cell reaches a density non-uniformity below 1% after 100 ms. The density equilibrium time, τ , scales with the ratio of cell volume to outlet area, a relationship that is not captured by the 2D simulations showing 5 times shorter equilibrium time. We present a method to determine τ from fluid simulations, allowing the estimation of the minimum delay required to enable a uniform target density. Such uniformity prevents uncontrolled electron injection from density ripples, which has direct implications for optimising beam quality and reproducibility in wakefield acceleration.

Keywords: computational fluid dynamics, particle accelerators

1. INTRODUCTION

Conventional radiofrequency (RF) cavity based accelerators are typically limited to 100 MVm⁻¹, constrained by cavity wall breakdown under strong fields^[1, 2]. Laser wakefield acceleration (LWFA) is a compact alternative for accelerating electrons in a plasma wave driven by a high-intensity laser^[3]. For the densities required, the plasma is usually produced from ionisation of an initially gaseous target. One method to make a suitable plasma is to use a capillary discharge, in which an electrical discharge flows through a gas-filled capillary^[4, 5]. Thermal balance with the capillary walls produces a plasma density channel which can serve to guide the laser over long lengths^[6]. Wakefield acceleration in capillary waveguides has produced acceleration of electrons to 8 GeV over 20 cm of plasma^[7]. However, capillary wave-guides are susceptible to laser-induced damage, particularly at high repetition-rates. Gas jets can produce targets ranging in density from 10^{23} to 10^{26} m^{-3[8]}. Supersonic jets^[9] enable the accelerator to be operated far from the gas jet nozzle, reducing damage issues. An alternative way to generate wave-guides is through the hydrodynamic expansion of optical field-ionised (HOFI) $plasmas^{[10-12]}$. This method has recently been used to accelerate electrons to 10 GeV in a 30 cm plasma formed in a gas jet $target^{[13]}$.

However, gas jets operate at significantly higher backing pressures, resulting in greater gas flow. This increased flow places a higher strain on the load of vacuum pumps and limits the system's repetition rate. The flow can suffer from stability issues due to turbulence. For a helium gas jet of nozzle throat diametre of 1 mm

and atomic density $1 \times 10^{25} \,\mathrm{m}^{-3}$, the Reynolds number

Gas cells are enclosed structures that confine a gas flow to produce a gaseous target^[16–19]. Gas cells can accommodate HOFI channels^[20], but can also be used for self-guided LWFA^[21]. This is where the non-linear response of the high intensity laser pulses enables them to be guided far beyond the length over which they would normally diffract^[22]. Gas cells are typically filled at a lower inlet pressure and have smaller exits for laser entry and exit. As such, the flow rates to reach the required densities are much slower and less prone to turbulence. Kuschel et al. investigated the dependence of the wavelength of the relativistic plasma wave, $\lambda_p \equiv 2\pi c/\omega_p$ along a fixed-length gas cell^[14]. They reported a gradient of $\partial_z \lambda_p = 0.25\%$ in gas cells, compared to $\partial_z \lambda_p = 3\%$ in gas jets. Their findings indicated that density ripples in gas jets caused strong structuring of the electron beam due to self-injection, whereas gas cells produced nearly unstructured beams with no uncontrolled injection.

Another advantage of gas cells is their ability to offer a tunable plasma length. By incorporating a piston, the plasma length in a gas cell can be precisely and rapidly adjusted, ranging from many centimetres down to a few hundred micrometres. This adjustability makes the gas cell suitable for operation across a wide range of densities, particularly as the distance required to reach maximum electron energy scales inversely with density. Additionally, this variable length allows for precise control of the acceleration distance over which electrons are accelerated. This enables the acceleration dynamics to be accurately determined and optimised^[23].

is ≈ 3400 assuming a flow speed of $1000\,\mathrm{ms}^{-1}$, which is in the transitional regime where turbulence begins to develop. It has been shown that small-scale density ripples over a distance of just a few plasma wave wavelengths can induce unwanted electron self-injection^[14], which leads to poor electron beam quality^[15].

^{*} runfeng.luo18@imperial.ac.uk

This peer-reviewed article has been accepted for publication but not yet copyedited or typeset, and so may be subject to change during the production process. The article is considered published and may be cited using its DOI.

This is an Open Access article, distributed under the terms of the Creative Commons Attribution licence (https://creativecommons.org/licenses/by/4.0/), which permits unrestricted re-use, distribution, and reproduction in any medium, provided the original work is properly cited.

However, care must be taken at the laser exit outlet of the gas cell. Sharp density transitions at this outlet can lead to unwanted degradation of beam emittance [24]. By using suitably engineered density ramps [25–27], it is possible to reduce the beam divergence and thus better preserve beam emittance. Being able to control the divergence of the beams produced in a LWFA is particularly important for many applications such as staged acceleration [28] or injection into undulators to produce radiation [29–31].

In this paper, we present simulations of a tunablelength gas cell to investigate the density uniformity and the time taken to reach equilibrium in the target. Understanding the evolution of the target density is critical for optimising the LWFA process, as the uniformity and shape of the density profile are crucial in producing highquality electron beams. Furthermore, an accurate estimation of the time to reach equilibrium provides insight into the density evolution. This is particularly important for the target design for high-repetition-rate LWFA operation, as high density uniformity is crucial for beam stability. We also explore the use an outlet designed as a converging-diverging nozzle. This generates longer exit density ramps which can be used to avoid rapid spread of the electron beam at the plasma exit^[24]. Since these regions are often difficult to diagnose experimentally, highfidelity density profile calculations will enable more accurate predictions of LWFA performance by providing precise inputs for PIC simulations.

2. COMPUTATIONAL FLUID DYNAMICS

To model the gas flow within the cell, computational fluid dynamics (CFD) simulations can be employed. However, CFD solvers face challenges when simulating vacuum conditions and extreme density variations^[32]. These abrupt density transitions can cause numerical oscillations, necessitating fine-tuning of ad-hoc parameters to achieve a stable solution. Such artificial parameter tuning becomes questionable for supersonic and transonic flows due to the lack of pointwise stability^[33]. 2D CFD simulations have been performed for a gas cell designed for density downramp injection^[16]. Extending these simulations to three dimensions is challenging, as the added geometrical complexity often leads to severe stability issues and substantially increased computational cost. Attempts have been made to simulate the gas cell using quasi-three-dimensional (r-z) geometries^[17], or using 3D geometries with a reduced volume, focusing on the outlet^[19]. However, performing a full 3D simulation that accurately captures the complete spatial and physical complexity of the gas cell system remains a substantial computational challenge.

For the simulations presented here, we use the code Ryujin, an open-source finite-element solver for conservation equations such as the compressible Navier-Stokes and Euler equations of gas dynamics^[33, 34]. The code

uses a convex limiting technique^[35] which guarantees admissibility in each time step by ensuring that the computed update maintains an invariant-domain property in each collocation point. Concretely, for the compressible Euler equations positivity of the density, positivity of the internal energy and a local minimum principle on the specific entropy are enforced^[35]. This limiting strategy guarantees robustness even under extreme shock conditions and for complex geometries, making Ryuiin particularly suitable for modelling scenarios with significant density variation, sharp transitions and real-life geometries such a gas cells for LWFA. The method is guaranteed to be stable without the use of any ad-hoc tuning parameters^[33, 35]. Owing to its convex limiting feature, Ryujin remains robust when simulating complex geometries, unlike other CFD methods that may experience divergence of physical quantities.

Ryujin's convex limiting algorithm blends an intermediate, robust, and viscous low-order update with a high-order update while maintaining the invariant-domain property. The intermediate low-order update is designed in such a way that it ensures that all thermodynamical constraints and entropy inequalities are maintained [36]. Ryujin accurately captures extreme density transitions, such as those occurring near vacuum boundaries, and is inherently stable against the divergence of physical quantities like temperature, a difficulty that often arises in other fluid simulations, particularly within complex 3D geometries. For further details about the underlying theory and implementation we refer the reader to [33, 35, 36].

3. SIMULATION SET-UP

The computational work is based on a gas cell designed for use as a wakefield accelerator utilising controlled ionisation injection $^{[15, 37-39]}$. It was optimised to produce low-divergence (< mrad), and low-emittance (< mm mrad) beams.

The cell is filled with helium gas, doped with a few percent of nitrogen by mass. The nitrogen K-shell electrons, which have a high ionisation threshold $(a_0 > 1)$, ionise only near the peak laser intensity^[15, 37–39]. Here, a_0 represents the normalised laser vector potential. Electrons ionised near this peak intensity can be generated with the optimal phase within the plasma bubble to remain trapped and accelerated^[40]. By adjusting the laser focus, the timing of the injection can be controlled to generate high-quality electron beams^[41].

The gas cell provides a helium atomic density ranging from 10^{23} to 10^{25} m⁻³, doped with a few percent of nitrogen by mass. To simplify the fluid simulations, and considering the low concentrations of nitrogen in the cell, our simulations assumed that the gas was pure helium.

A cone with a $400\,\mu m$ diametre hole serves as the aperture through which the laser enters the cell. The dimensions of the cone were selected as a compromise between achieving a higher operating density and min-

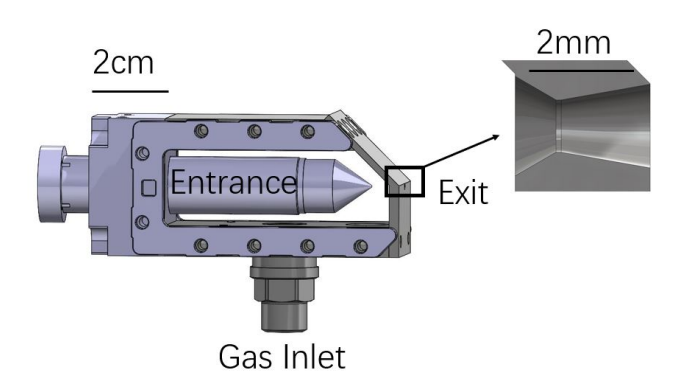


FIG. 1: A CAD rendering of the cell geometry along with a zoomed-in view of the nozzle at the laser exit.

imising laser-induced damage to the outlet. As shown in FIG. 1, the cone is mounted on a piston that allows the aperture position to be adjusted along the laser beam axis while maintaining the gas cell seal, providing control over the target length. The cell is $5.9\,\mathrm{cm}$ in length with a volume of $38\,\mathrm{cm}^3$. The piston is oriented towards the laser entrance to facilitate rapid downstream access for applications such as staged acceleration.

To introduce the density down-ramp, the exit aperture is shaped into a converging-diverging nozzle, approximating de Laval nozzles that are used for accelerating fluids to supersonic speed^[42]. The resulting longer ramps would help collimate the naturally divergent electron beams produced by LWFA. FIG. 1 includes a detailed view of the converging-diverging nozzle. The converging section began with a diameter of 1.9 mm and extended 0.8 mm in length. The throat section measured 1.0 mm in diameter and 0.1 mm in length. The diverging section extended 1.7 mm, widening to a final diameter of 1.6 mm.

Ryujin defines the initial conditions on either side of the inlet interface using two sets of primitive states. A primitive state refers to a set of physical parameters that describe the fluid at a given point, including density, thermal velocity, and pressure. In this study, we simulated pure helium with an inlet pressure of 100 mbar. The density was determined using the ideal gas law, assuming a temperature of 300 K. The velocity of the primitive state corresponds to the mean thermal velocity of gas particles as derived from the Boltzmann distribution. The initial vacuum pressure was assumed to be 10^{-5} mbar.

The Knudsen number, Kn, is the ratio of the molecular mean free path to the physical scale in the system. It characterises the type of the flow. For Kn < 0.01, the continuum flow assumption is valid, and the no-slip boundary condition applies. For 0.01 < Kn < 0.1, the velocity slip at the wall becomes important, and the slip boundary conditions should be used^[43]. The Knudsen number for helium at 300 K and 100 mbar, with the nozzle throat as the smallest length scale at $0.1 \, \mathrm{mm}$ is approximately 0.0138. This value indicates that the gas

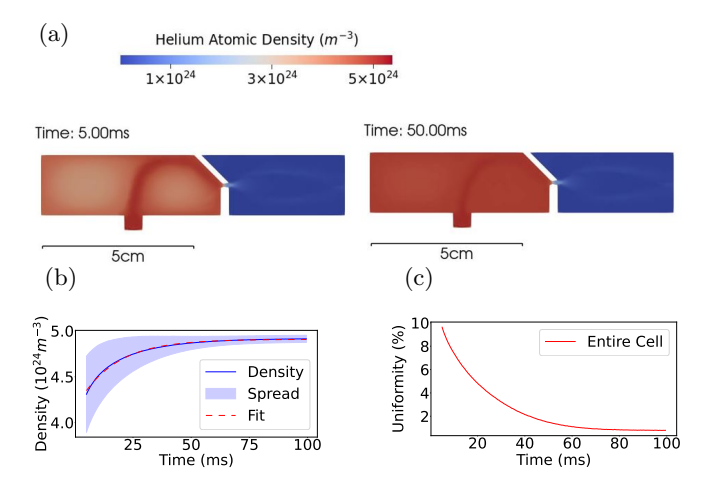


FIG. 2: Helium atomic density distribution and uniformity for the 2D cell without piston. (a) Transverse slices of the density distribution at 5 and 50 ms. (b) Mean helium atomic density in the gas cell as a function of time after gas release. (c) Temporal evolution of density uniformity (standard deviation) in the gas cell.

flow in the cell is within the slip-flow regime, and consequently, for these simulations, the wall conditions were set to slip.

4. SIMULATION RESULTS

To evaluate the capability of Ryujin, we first conducted 2D trial simulations using a simplified geometry without the piston. FIG. 2a) shows transverse slices of the density distribution at 5 and 50 ms after gas release. At 5 ms, the system had not yet reached equilibrium, and a higher density is found near the inlet. By 50 ms, the density had stabilised and become uniform. As shown in FIG. 2b), the density plateaued at $4.91 \times 10^{25} \, \mathrm{m}^{-3}$ after 50 ms. An exponential fit to the mean density reveals a characteristic time of 16 ms.

FIG. 3 presents the results of the 2D simulation, including the trombone, as implemented in the variablelength gas cell. The distance from the trombone to the outlet was set to 9 mm. FIG. 3a) shows transverse slices of the density distribution at 5 and 50 ms after gas release, which also illustrate the cell geometry. The cell comprised an inlet at the bottom and a piston inside. The outlet on the piston was neglected, as this area was significantly smaller compared to the nozzle size. The right wall served as the outlet. At 5 ms, the flow is again quite non-uniform, but the mean density is observed to have stabilised at $4.24 \times 10^{25} \,\mathrm{m}^{-3}$ after $40 \,\mathrm{ms}$, as shown in FIG. 3b). The density evolution indicated a characteristic time of 9.3 ms. The density inhomogeneity in the LWFA region, defined as a cylindrical volume within the cell with a radius twice that of the outlet and centred along the laser direction, decreased to below 1% after

15 ms, as shown in FIG. 3c). However, the density inhomogeneity across the entire cell remains above 15%, at 50 ms. As illustrated in FIG. 3a), density gradients persist in the top left corner even after the mean density throughout the cell has stabilised. The complex geometry of the cell obstructs fluid flow to the corners, thereby leading to persistent non-uniformities in the density distribution. Additionally, the presence of the piston results in a reduced characteristic time, attributed to the smaller effective volume compared to configurations without the piston.

While 2D simulations provide useful insights into general flow behaviour, they inherently lack the ability to capture the full spatial complexity of gas dynamics within the cell. Transitioning to 3D simulation is crucial for further investigation of the density equilibrium time and the density inhomogeneities caused by the cell's geometry and outlet configuration, but the complex geometry increases the computational difficulty. The 3D finite element mesh requires particular consideration. Currently, Ryujin only accepts quadrilateral and hexahedral mesh elements. While tetrahedral meshing offers greater flexibility for handling complex geometries, it is prone to numerical diffusion, particularly when modelling shocks and sharp density transitions^[44]. By contrast, the hexahedral mesh provides higher accuracy, but generating a fine mesh for complex geometries is challenging. For simplification, the cylindrical piston was replaced by a hexagonal-shaped rod inside the cell. Additionally, the cones defining the converging-diverging nozzles were approximated using polygons, while squares were used to represent the outlet, reducing computational time. A three-dimensional finite element mesh generator, known

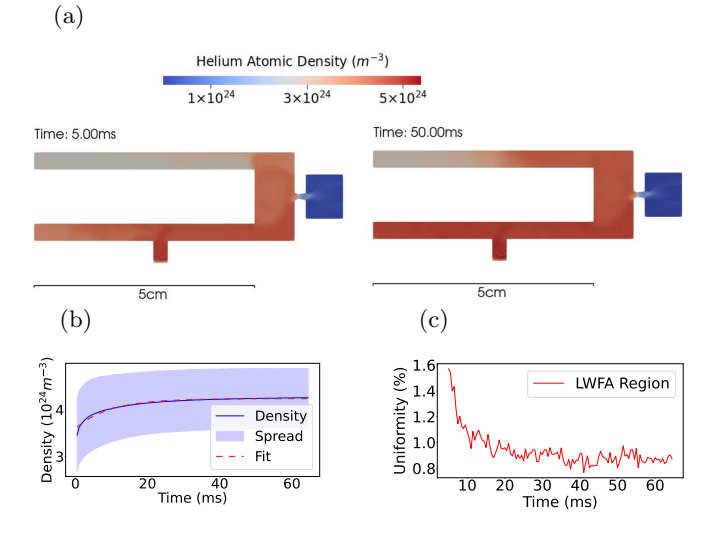


FIG. 3: Helium atomic density distribution and uniformity for the 2D cell geometry with piston. (a) Transverse slices of the density distribution at 5 and 50 ms. (b) Mean helium atomic density in the gas cell as a function of time after gas release. (c) Temporal evolution of density uniformity (standard deviation) in the LWFA region.

as Gmsh^[45], was used to generate the Ryujin inputs. It features the ability to force the mesh elements to be hexahedral, and 3D volume meshes were created as a compromise between the mesh quality and the computation time. The simulations were performed on the Imperial HPC system with 8 Icelake CPU cores^[46]. It took a day to compute 300 ms for the 3D simulations, compared to a few hours for the 2D simulations. The 3D mesh resolution resulted in about 35,000 collocation points, which amounted to 175,000 total spatial degrees of freedom.

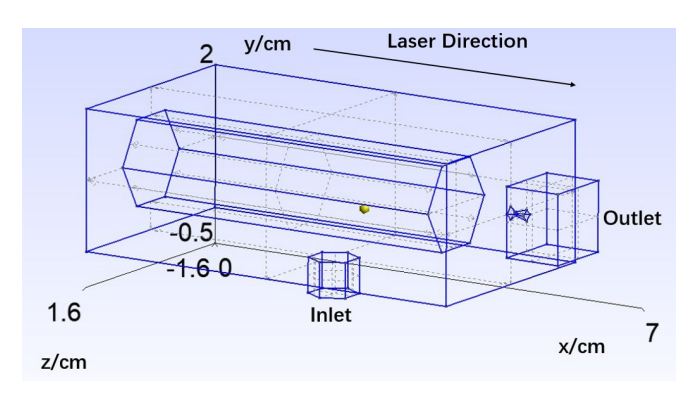


FIG. 4: Visualisation of the 3D cell geometry in Gmsh.

FIG. 4 presents the gas cell geometry used for the 3D simulation. FIG. 5a) displays transverse slices of the density distribution at 5 ms and 300 ms after gas release. As observed in 2D simulations, the density within the cell becomes uniform upon reaching equilibrium. The mean density inside the cell was projected to plateau at $5.02\times10^{24}\,\mathrm{m}^{-3}$, as shown in FIG. 5b). The characteristic time for the density increase was 56 ms, and the density non-uniformity within the cell decreased below 1% after 100 ms, as depicted in FIG. 5c). FIG. 5c) also compares the density non-uniformity in both the entire cell and the LWFA region. The LWFA region exhibited smaller final density spread. After the initial fluctuation, the density spread plateaued at 1% beyond 40 ms.

The characteristic time scale, τ , represents the exponential time constant for density stabilisation. Achieving uniformity within 1% requires approximately two to three characteristic time periods. This time determines the minimum laser delay necessary to ensure a uniform density. The characteristic time can be estimated as the ratio of the fluid mass contained within the cell to the mass flow rate exiting through the nozzle, given by [47]:

$$\tau = \frac{V}{C_d A_{out}} \sqrt{\frac{\rho_0}{2\Delta P}},\tag{1}$$

where ρ_0 is the mass density, and ΔP is the pressure difference between the cell and the vacuum. The volume of the cell and the area of the outlet are denoted by V and A_{out} , respectively. When the inlet size is significantly larger than the outlet, the gas fills the cell on a timescale that is much shorter than the density equilibrium time.

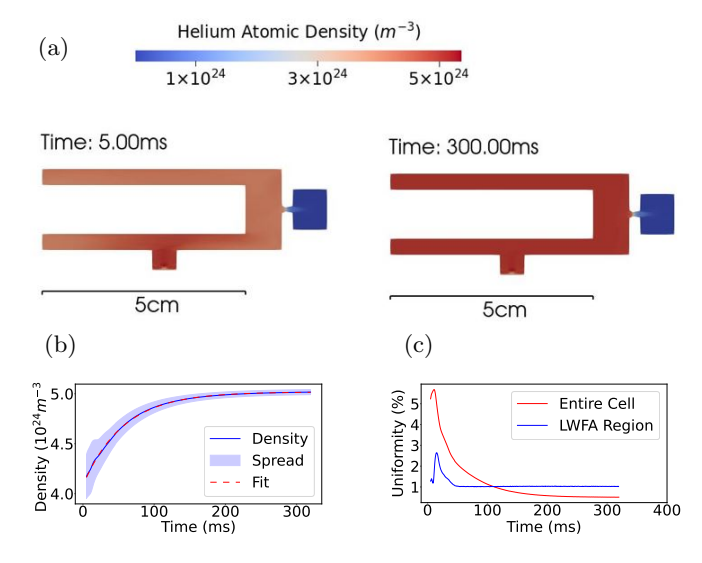


FIG. 5: Helium atomic density distribution and uniformity for the 3D cell geometry. (a) Transverse slices of the density distribution at 5 and 300 ms. (b) Mean helium atomic density in the entire cell and in the LWFA region as a function of time after gas release. (c) Temporal evolution of density uniformity (standard deviation) in the entire cell and the LWFA region.

Although the initial filling dynamics of an empty gas cell are strongly governed by the inlet area, the outlet size ultimately determines the rate at which the system approaches density equilibrium. Here, C_d is the discharge coefficient, which is close to unity for a nozzle^[48].

	τ_{sim} (ms)	$\tau_{theory} \; (\mathrm{ms})$	$\delta \tau / \tau$ (%)
2D (no piston)	16	1.0	94
2D (with piston)	9.3	0.52	94
3D	56.1	56.8	1.2

TABLE I: Comparison of the equilibrium time obtained from simulations (τ_{sim}) with the theoretical value (τ_{theory}) predicted by Eq. 1, along with the percentage difference between them.

Tab. I summarises the equilibrium times obtained from the simulations, alongside the values predicted by Eq. 1, assuming the outlet size of 1 mm, equivalent to the throat size. Eq. 1 accurately predicts the equilibrium time in 3D simulations, with deviations at the percent level.

In the 2D simulations, the case with the piston exhibited a shorter equilibrium time compared to the case without the piston, as expected from theoretical predictions, due to the smaller effective cell volume. However, in 2D, the concept of volume becomes ambiguous. The 2D model effectively assumes the cell extends infinitely in the direction perpendicular to the simulation plane, such that the influence of the third dimension is negligible. As a result, the volume-to-outlet area ratio reduces

to the ratio of the cell's cross-sectional area to the outlet length. Eq. 1 can then be reformulated as:

$$\tau_{3d} = \tau_{2d} \frac{2L_{cell}}{\pi r_{out}},\tag{2}$$

 L_{cell} is the length of the cell in the direction perpendicular to the plane of the 2D simulation. Based on this relation, FIG. 5b) is expected to show a characteristic time 40 times larger than in FIG. 3b). A longer equilibrium time was observed in 3D as compared to 2D. However, the predicted time for the 2D case was almost an order of magnitude lower than the computational results. This discrepancy arises from the complex internal geometry of the gas cell, which the simplified model does not fully account for. As shown in FIG. 3b), the upper section of the gas cell is connected to the inlet only via a narrow path around the piston tip, which restricts gas flow and leads to a prolonged equilibrium time. By contrast, in 3D the gas flow from the inlet is less obstructed, resulting in a shorter equilibrium time that differs by only 1.5% from the theoretical prediction. The 3D fluid simulation, combined with the theoretical model, provides an accurate estimation of the density equilibrium time for the gas cell target. This capability is readily extendable to arbitrary gas cell targets and even other types of LWFA targets, thereby aiding target design by providing reliable equilibrium time estimates. Owing to the convex limiting feature, Ryujin remains robust when simulating complex geometries, which broadens the applicability of Ryujin to a wide range of wakefield targets.

The cell studied here exhibits a characteristic recovery time of approximately 56 ms, with density equilibrium established between 100 ms and 200 ms. This corresponds to a maximum repetition rate of 5-10 Hz. The transverse cross-section of the cell is about 3 cm by 2 cm. If reduced to 1 cm by 1 cm or less, the repetition rate could increase by a factor of 6 to 10. The outlet area can also be increased, albeit at the cost of a shorter density ramp length. Such a cell would be well suited for high-repetition-rate LWFA.

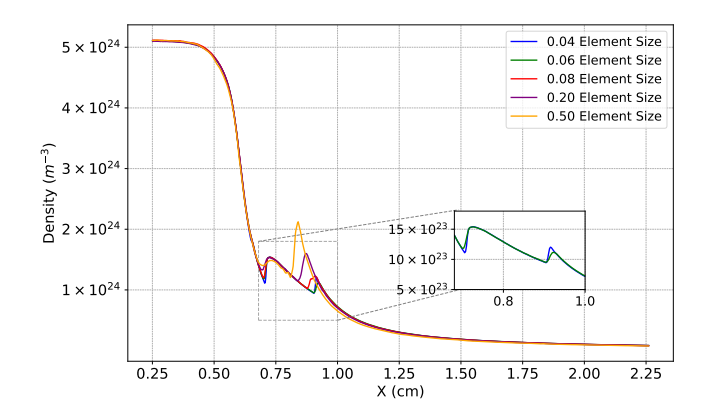


FIG. 6: Convergence scan of the density downramp profile using 2D simulations.

To investigate the density downramp, we conducted a 2D convergence study of the density profile using a reduced geometry consisting of only the outlet nozzle. FIG. 6 compares the on-axis density profile along the downramp for different mesh resolutions, characterised by the element size factor. This factor represents the element size relative to the characteristic Gmsh size, which is heuristically determined as a fraction of the geometry's bounding box size and further refined based on the smallest geometric features. All the simulations with varying element sizes produced the same uniform density within the gas cell and a consistent downramp profile for $0.25\,\mathrm{cm} < x < 0.75\,\mathrm{cm}$. This indicates that the mesh resolution does not significantly influence the density plateau or the ramp scale-length. However, for a coarse mesh an artificial thickness is assigned to the density bump that forms at the location where the shockwaves, generated by discontinuities in the nozzle, rejoin. The inset in FIG. 6 reveals that the density profile begins to converge at an element size of 0.06. While this does not alter the gas flow within the cell, a fine mesh resolution is necessary to accurately capture the key features of the supersonic flows emerging from the nozzles. The peak density of the bump is orders of magnitude lower than the plateau density, as show in FIG. 6. Hence, this feature is not expected to significantly influence the dynamics of the wakefield accelerator.

To characterise the length of the density downramp, an analytical function of the form:

$$\rho = \rho_0 \left(e^{-x/\lambda} + 1 \right)^{-1},\tag{3}$$

was fitted to the on-axis density lineout for the fluid simulation with an element size of 0.06. Here, ρ_0 is the plateau density, while λ represents the scale-length of the ramp. For a circular outlet, the scale-length λ is approximately R/2, where R is the outlet radius. In the case of a nozzle with a tailored nozzle with a throat radius of 0.5 mm, the ramp scale-length was found to be extended to 0.32 mm^[24]. The converging-diverging nozzle geometry, combined with the large aperture size, contributes to an extended scale-length. Such extended ramps could be beneficial in reducing electron beam

divergence from the LWFA^[24]. However, obtaining experimental measurements of density profiles near the gas outlets are usually obscured by the metallic and opaque nozzle structure. This makes it difficult to have accurate measurements of this region where critical dynamics take place. Hence, integrating the results from these fluid simulations with PIC simulations provides a powerful approach to investigate density downramps and their role in generating low-divergence electron beams. This is vital for practical applications such as wakefield-based free-electron lasers^[31].

5. CONCLUSIONS

We performed hydrodynamics simulations of a variable length gas cell. For both 2D and 3D simulations, the standard deviation of the density fell below 1%, indicating high density uniformity for a cell target. This would help to reduce uncontrolled self-injection due to density ripples on the scale of the plasma wave wavelength, demonstrating that a gas cell target offers finer density control as compared to a gas jet. Our results show that 2D simulations underestimate the true equilibrium time by a factor of 5 times. This highlights the importance of 3D simulations for accurately determining the equilibrium time of the cell, a task for which the Ryujin simulations are well-suited. The simulation is adaptable to arbitrary LWFA targets, and the code enables robust studies of gas dynamics in complex targets, free from stability issues. The 3D simulation shows a characteristic time of 56 ms for a gas cell with a volume of 38 cm³, and predict that the density variation inside the cell drops below 1% after 100 ms. Such a cell would thus be unsuitable for use in pulsed mode for high-repetition-rate LWFA. However, our modeling and eq. 1 indicates that the design of a smaller cell volume would have smaller equilibrium times. Ryujin simulations, combined with eq. 1, can be used to design a gas cell target appropriate for LWFA operation at 10 Hz.

The authors acknowledge funding from STFC (ST/J002062/1, ST/P002021/1, ST/V001639/1), and support from the Imperial College Research Computing Service.

S. Döbert and M. Park, Gradient limitations for high-frequency accelerators, Proceedings of LINAC 2004, 513 (2004).

^[2] E. Senes, T. Argyropoulos, F. Tecker, and W. Wuensch, Beam-loading effect on breakdown rate in high-gradient accelerating cavities: An experiment at the Compact Linear Collider Test Facility at CERN, Physical Review Accelerators and Beams 21, 102001 (2018).

^[3] T. Tajima and J. M. Dawson, Laser electron accelerator, Physical Review Letters 43, 267 (1979).

^[4] D. J. Spence, A. Butler, and S. M. Hooker, Gas-filled capillary discharge waveguides, J. Opt. Soc. Am. B 20,

^{138 (2003).}

^[5] S. Karsch, J. Osterhoff, A. Popp, T. P. Rowlands-Rees, Z. Major, M. Fuchs, B. Marx, R. Hörlein, K. Schmid, L. Veisz, S. Becker, U. Schramm, B. Hidding, G. Pretzler, D. Habs, F. Grüner, F. Krausz, and S. M. Hooker, Gevscale electron acceleration in a gas-filled capillary discharge waveguide, New Journal of Physics 9, 415 (2007).

^[6] A. Butler, D. J. Spence, and S. M. Hooker, Guiding of high-intensity laser pulses with a hydrogen-filled capillary discharge waveguide, Phys. Rev. Lett. 89, 185003 (2002).

^[7] A. J. Gonsalves, K. Nakamura, J. Daniels, C. Benedetti, C. Pieronek, T. C. D. Raadt, S. Steinke, J. H. Bin, S. S.

- Bulanov, J. V. Tilborg, C. G. Geddes, C. B. Schroeder, C. Tóth, E. Esarey, K. Swanson, L. Fan-Chiang, G. Bagdasarov, N. Bobrova, V. Gasilov, G. Korn, P. Sasorov, and W. P. Leemans, Petawatt laser guiding and electron beam acceleration to 8 GeV in a laser-heated capillary discharge waveguide, Physical Review Letters 122, 084801 (2019).
- [8] A. M. Hansen, D. Haberberger, J. Katz, D. Mastrosimone, R. K. Follett, and D. H. Froula, Supersonic gas-jet characterization with interferometry and Thomson scattering on the OMEGA Laser System, Review of Scientific Instruments 89, 10C103 (2018).
- [9] S. Semushin and V. Malka, High density gas jet nozzle design for laser target production, Review of Scientific Instruments 72, 2961 (2001).
- [10] N. Lemos, T. Grismayer, L. Cardoso, J. Geada, G. Figueira, and J. M. Dias, Effects of laser polarization in the expansion of plasma waveguides, Physics of Plasmas 20, 103109 (2013).
- [11] N. Lemos, T. Grismayer, L. Cardoso, G. Figueira, R. Issac, D. A. Jaroszynski, and J. M. Dias, Plasma expansion into a waveguide created by a linearly polarized femtosecond laser pulse, Physics of Plasmas 20, 063102 (2013).
- [12] R. J. Shalloo, C. Arran, L. Corner, J. Holloway, J. Jonnerby, R. Walczak, H. M. Milchberg, and S. M. Hooker, Hydrodynamic optical-field-ionized plasma channels, Physical Review E 97, 053203 (2018).
- [13] A. Picksley, J. Stackhouse, C. Benedetti, K. Nakamura, H. E. Tsai, R. Li, B. Miao, J. E. Shrock, E. Rockafellow, H. M. Milchberg, C. B. Schroeder, J. van Tilborg, E. Esarey, C. G. R. Geddes, and A. J. Gonsalves, Matched guiding and controlled injection in darkcurrent-free, 10-GeV-class, channel-guided laser-plasma accelerators, Phys. Rev. Lett. 133, 255001 (2024).
- [14] S. Kuschel, M. B. Schwab, M. Yeung, D. Hollatz, A. Seidel, W. Ziegler, A. Sävert, M. C. Kaluza, and M. Zepf, Controlling the self-injection threshold in laser wakefield accelerators, Physical Review Letters 121, 154801 (2018).
- [15] S. Bohlen, J. C. Wood, T. Brümmer, F. Grüner, C. A. Lindstrøm, M. Meisel, T. Staufer, R. D'Arcy, K. Põder, and J. Osterhoff, Stability of ionization-injection-based laser-plasma accelerators, Physical Review Accelerators and Beams 25, 031301 (2022).
- [16] O. Kononenko, N. C. Lopes, J. M. Cole, C. Kamperidis, S. P. Mangles, Z. Najmudin, J. Osterhoff, K. Poder, D. Rusby, D. R. Symes, J. Warwick, J. C. Wood, and C. A. Palmer, 2D hydrodynamic simulations of a variable length gas target for density down-ramp injection of electrons into a laser wakefield accelerator, Nuclear Instruments and Methods in Physics Research, Section A: Accelerators, Spectrometers, Detectors and Associated Equipment 829, 125 (2016).
- [17] T. L. Audet, P. Lee, G. Maynard, S. D. Dufrénoy, A. Maitrallain, M. Bougeard, P. Monot, and B. Cros, Gas cell density characterization for laser wakefield acceleration, Nuclear Instruments and Methods in Physics Research, Section A: Accelerators, Spectrometers, Detectors and Associated Equipment 909, 383 (2018).
- [18] C. Aniculaesei, H. T. Kim, B. J. Yoo, K. H. Oh, and C. H. Nam, Novel gas target for laser wakefield accelerators, Review of Scientific Instruments 89, 10.1063/1.4993269 (2018).
- [19] P. Drobniak, E. Baynard, A. Beck, J. Demailly, D. Douil-

- let, A. Gonnin, G. Iaquaniello, G. Kane, S. Kazamias, V. Kubytskyi, M. Lenivenko, N. Lericheux, B. Lucas, B. Mercier, Y. Peinaud, M. Pittman, J. Serhal, and K. Cassou, Two-chamber gas target for laser-plasma electron source, Review of Scientific Instruments **96**, 033304 (2025).
- [20] S. M. Mewes, G. J. Boyle, A. F. Pousa, R. J. Shalloo, J. Osterhoff, C. Arran, L. Corner, R. Walczak, S. M. Hooker, and M. Thévenet, Demonstration of tunability of HOFI waveguides via start-to-end simulations, Physical Review Research 5, 033112 (2023).
- [21] J. Osterhoff, A. Popp, Z. Major, B. Marx, T. P. Rowlands-Rees, M. Fuchs, M. Geissler, R. Hörlein, B. Hidding, S. Becker, E. A. Peralta, U. Schramm, F. Grüner, D. Habs, F. Krausz, S. M. Hooker, and S. Karsch, Generation of stable, low-divergence electron beams by laser-wakefield acceleration in a steady-state-flow gas cell, Physical Review Letters 101, 085002 (2008).
- [22] A. G. R. Thomas, Z. Najmudin, S. P. D. Mangles, C. D. Murphy, A. E. Dangor, C. Kamperidis, K. L. Lancaster, W. B. Mori, P. A. Norreys, W. Rozmus, and K. Krushelnick, Effect of laser-focusing conditions on propagation and monoenergetic electron production in laser-wakefield accelerators, Phys. Rev. Lett. 98, 095004 (2007).
- [23] K. Põder, J. C. Wood, N. C. Lopes, J. M. Cole, S. Alatabi, M. P. Backhouse, P. S. Foster, A. J. Hughes, C. Kamperidis, O. Kononenko, S. P. D. Mangles, C. A. J. Palmer, D. Rusby, A. Sahai, G. Sarri, D. R. Symes, J. R. Warwick, and Z. Najmudin, Multi-GeV electron acceleration in wakefields strongly driven by oversized laser spots, Phys. Rev. Lett. 132, 195001 (2024).
- [24] M. Backhouse, Measurement and optimisation of beam quality from laser wakefield accelerators, Ph.D. thesis, Imperial Coll., London (2022).
- [25] C. B. Schroeder, E. Esarey, C. Benedetti, and W. P. Leemans, Control of focusing forces and emittances in plasma-based accelerators using near-hollow plasma channels, Physics of Plasmas 20, 080701 (2013).
- [26] M. D. Litos, R. Ariniello, C. E. Doss, K. Hunt-Stone, and J. R. Cary, Beam emittance preservation using gaussian density ramps in a beam-driven plasma wakefield accelerator, Philosophical Transactions of the Royal Society A: Mathematical, Physical and Engineering Sciences 377, 20180181 (2019).
- [27] Y. Zhao, W. An, X. Xu, F. Li, L. Hildebrand, M. J. Hogan, V. Yakimenko, C. Joshi, and W. B. Mori, Emittance preservation through density ramp matching sections in a plasma wakefield accelerator, Physical Review Accelerators and Beams 23, 011302 (2020).
- [28] S. Steinke, J. V. Tilborg, C. Benedetti, C. G. Geddes, C. B. Schroeder, J. Daniels, K. K. Swanson, A. J. Gonsalves, K. Nakamura, N. H. Matlis, B. H. Shaw, E. Esarey, and W. P. Leemans, Multistage coupling of independent laser-plasma accelerators, Nature 530, 190 (2016).
- [29] H. P. Schlenvoigt, K. Haupt, A. Debus, F. Budde, O. Jäckel, S. Pfotenhauer, H. Schwoerer, E. Rohwer, J. G. Gallacher, E. Brunetti, R. P. Shanks, S. M. Wiggins, and D. A. Jaroszynski, A compact synchrotron radiation source driven by a laser-plasma wakefield accelerator, Nature Physics 4, 130–133 (2008).
- [30] M. Fuchs, R. Weingartner, A. Popp, Z. Major, S. Becker, J. Osterhoff, I. Cortrie, B. Zeitler, R. Hörlein, G. D. Tsakiris, U. Schramm, T. P. Rowlands-Rees, S. M.

- Hooker, D. Habs, F. Krausz, S. Karsch, and F. Grüner, Laser-driven soft-X-ray undulator source, Nature Physics 5, 826–829 (2009).
- [31] W. Wang, K. Feng, L. Ke, C. Yu, Y. Xu, R. Qi, Y. Chen, Z. Qin, Z. Zhang, M. Fang, J. Liu, K. Jiang, H. Wang, C. Wang, X. Yang, F. Wu, Y. Leng, J. Liu, R. Li, and Z. Xu, Free-electron lasing at 27 nanometres based on a laser wakefield accelerator, Nature 595, 516 (2021).
- [32] C. Liu, G. Zhou, W. Shyy, and K. Xu, Limitation principle for computational fluid dynamics, Shock Waves 29, 1083–1102 (2019).
- [33] M. Maier and M. Kronbichler, Efficient parallel 3D computation of the compressible Euler equations with an invariant-domain preserving second-order finite-element scheme, ACM Transactions on Parallel Computing 8, 16:1 (2021).
- [34] J.-L. Guermond, M. Kronbichler, M. Maier, B. Popov, and I. Tomas, On the implementation of a robust and efficient finite element-based parallel solver for the compressible Navier-stokes equations, Computer Methods in Applied Mechanics and Engineering 389, 114250 (2022).
- [35] J.-L. Guermond, M. Nazarov, B. Popov, and I. Tomas, Second-order invariant domain preserving approximation of the euler equations using convex limiting, SIAM J. Sci. Comput. 40, A3211 (2018).
- [36] J.-L. Guermond and B. Popov, Invariant domains and first-order continuous finite element approximation for hyperbolic systems, SIAM J. Numer. Anal. 54, 2466 (2016).
- [37] T. P. Rowlands-Rees, C. Kamperidis, S. Kneip, A. J. Gonsalves, S. P. D. Mangles, J. G. Gallacher, E. Brunetti, T. Ibbotson, C. D. Murphy, P. S. Foster, M. J. V. Streeter, F. Budde, P. A. Norreys, D. A. Jaroszynski, K. Krushelnick, Z. Najmudin, and S. M. Hooker, Laser-driven acceleration of electrons in a partially ionized plasma channel, Phys. Rev. Lett. 100, 105005 (2008).
- [38] C. McGuffey, A. G. R. Thomas, W. Schumaker, T. Matsuoka, V. Chvykov, F. J. Dollar, G. Kalintchenko, V. Yanovsky, A. Maksimchuk, K. Krushelnick, V. Y. Bychenkov, I. V. Glazyrin, and A. V. Karpeev, Ionization

- induced trapping in a laser wakefield accelerator, Phys. Rev. Lett. **104**, 025004 (2010).
- [39] A. Pak, K. A. Marsh, S. F. Martins, W. Lu, W. B. Mori, and C. Joshi, Injection and trapping of tunnelionized electrons into laser-produced wakes, Physical Review Letters 104, 025003 (2010).
- [40] M. Chen, E. Esarey, C. B. Schroeder, C. G. Geddes, and W. P. Leemans, Theory of ionization-induced trapping in laser-plasma accelerators, Physics of Plasmas 19, 033101 (2012).
- [41] J. Wang, J. Feng, C. Zhu, Y. Li, Y. He, D. Li, J. Tan, J. Ma, and L. Chen, Small energy spread electron beams from laser wakefield acceleration by self-evolved ionization injection, Plasma Physics and Controlled Fusion 60, 034004 (2018).
- [42] N. D. Deshpande, S. S. Vidwans, P. R. Mahale, R. S. Joshi, and K. R. Jagtap, Theoretical CFD analysis of De Laval nozzle, 4th IRF International Conference 5, 61 (2014).
- [43] L. Zhang, S. Baochao, Z. Yulong, and G. Zhaoli, Review of micro seepage mechanisms in shale gas reservoirs, International Journal of Heat and Mass Transfer 139, 144 (2019).
- [44] K. Kotrasova and V. Michalcova, The study of the numerical diffusion in computational calculation, MATEC Web of Conferences 310, 00039 (2020).
- [45] J. Geuzaine and C. Remacle, Gmsh: a three-dimensional finite element mesh generator with built-in pre- and postprocessing, Facilities. Int. J. Numer. Meth. Eng. 79, 1309 (2009).
- [46] Imperial College Research Computing Service, Imperial College Research Computing Service, accessed: 2024-09-06.
- [47] A. Golijanek-Jedrzejczyk, D. Świsulski, R. Hanus, M. Zych, and L. Petryka, Uncertainty of the liquid mass flow measurement using the orifice plate, Flow Measurement and Instrumentation 62, 84 (2018).
- [48] J. Woodward, Source modeling discharge rates, in Reference Module in Chemistry, Molecular Sciences and Chemical Engineering (Elsevier, 2014).